Tropical precipitation variability and convectively coupled equatorial waves on submonthly time-scales in reanalyses and TRMM

JI-EUN KIM

Department of Atmospheric and Oceanic Sciences, University of Colorado, Boulder, Colorado

M. JOAN ALEXANDER

NorthWest Research Associates/CoRA, Boulder, Colorado

Submitted June 15, 2012

Revised October XX, 2012

ABSTRACT

Tropical precipitation characteristics are investigated using the Tropical Rainfall Measuring Mission (TRMM) 3-hourly estimates, and the result is compared with five reanalyses including ERA-interim (ERA), Modern-Era Retrospective Analysis (MERRA), National Centers for Environmental Prediction (NCEP)-National Center for Atmospheric Research (NCEP1), NCEP-Department of Energy (NCEP2), and NCEP-Climate Forecast System Reanalysis (CFSR). Precipitation characteristics are evaluated in terms of the mean, convectively coupled equatorial wave (CCEW) activity, frequency characteristics, diurnal cycle, and seasonality of regional precipitation variability associated with submonthly scale waves. Generally the latest reanalyses such as ERA, MERRA, and CFSR show better performances over NCEP1 and NCEP2. However, all the reanalyses are still different from observations. Besides the positive mean bias in the reanalyses, a spectral analysis revealed that the reanalyses have over-reddened spectra with persistent rainfall. MERRA has the most persistent rainfall, and CFSR appears to have the most realistic variability. The diurnal cycle in NCEP1 is extremely exaggerated compared to TRMM. The low-frequency CCEWs with the period longer than 3 days are well represented in ERA, MERRA, and CFSR, but all the reanalyses have significant deficiencies in representing CCEWs and variability in the high-frequency scale.

1. Introduction

Tropical convection plays a vital role in global climate by driving large-scale circulation, releasing latent heat, modulating radiative forcing, and most importantly redistributing water in the earth system. Due to complex interactions of moist convection with dynamical, thermodynamical, and cloud processes, it is difficult to fully understand the tropical precipitation system. Over the past few decades, global observations with the advent of satellites have enabled better understanding of how tropical convection is organized and evolves. Studies about cloudiness and precipitation have revealed that tropical convective systems are often organized by equatorial waves, rather than initiated randomly (Cho et al. 2004; Wheeler and Kiladis 1999). The equatorial waves trigger moist convection, and at the same time the tropical convection itself generates waves that propagate horizontally and vertically. These intriguing inter-dynamical responses between convection and equatorial waves occur at broad temporal and spatial scales ranging from the mesoscale to the planetary scale.

The pronounced spectral peaks in the observed equatorial waves correspond to the predicted dispersion curves, solutions of the shallow water equations on the equatorial beta plane (Matsuno 1966). As mathematically derived by Matsuno, observations have confirmed the existence of equatorial waves such as the Kelvin, mixed Rossby-Gravity (MRG), equatorial Rossby, and inertio-gravity (IG) waves (Kiladis et al. 2009). In addition to these waves, the Madden-Julian Oscillation (MJO) and tropical depression (TD)-type waves (Takayabu and Nitta 1993) also have significant impact on tropical weather and climate by coupling with convection. The MJO is the eastward propagating convective envelope, dominating intraseasonal (30-90 days) variability with the speed of about 5 m/s (Zhang 2005). Within the active phase of the MJO, a broad spectrum of cloud clusters coupled with waves has been identified. The tropical depression (TD)-type waves, also known as “easterly waves”, are westward propagating synoptic scale disturbances along the ITCZ with periods of 2-6 days—predominantly 3-6 days—and speeds of 5-10 m/s (Frank and Roundy 2006; Kiladis et al. 2006; Dickinson and Molinari 2002). This type of wave is very important for the formation of tropical cyclones (Frank and Roundy 2006).

In addition to direct impacts of CCEWs on tropical weather, indirect effects of convection are also significant for the tropical middle atmosphere and global climate. Observational studies of meteorological variables have discovered the existence of equatorial waves in the stratosphere (Wallace and Kousky 1968; Yanai and Maruyama 1966). These waves are called dry or free waves, because although they are generated by latent heating due to tropospheric moist convection they are no longer coupled with convection as they propagate into the upper atmosphere (Holton 1972). More vertically propagating waves are preferentially excited by small and transient scale convection (Alexander and Holton 2004). The prime example of the dry wave impacts is the forcing of the QBO, which is a quasi-periodic downward propagation of easterly and westerly zonal flows (Baldwin et al. 2001). By depositing easterly and westerly momentum in the stratosphere, vertically propagating waves modulate the background zonal wind (Alexander and Holton 1997; Kawatani et al. 2010; Lindzen and Holton 1968). Also, the tropical waves are partially responsible for driving the global-scale stratospheric transport circulation. Redistribution of important chemical constituents such as ozone and water vapor by this circulation modulates the tropospheric and stratospheric climate (Forster and Shine 2002; Hegglin and Shepherd 2009; Solomon et al. 2010).

Hence, generating realistic precipitation variability and CCEWs in climate simulation models is a fundamental problem in correct prediction of middle atmosphere climate as well as in accurate weather forecasting. Despite its importance, precipitation in current climate simulations shows large disagreements among different models. Studies have revealed that many general circulation models (GCMs) still do not produce CCEWs properly (Lin et al. 2006; Straub et al. 2010). Moreover, most of the studies have been conducted only for intraseasonal scale variability.

Evaluation studies of precipitation have also been conducted for reanalyses (Betts et al. 2006; Bosilovich et al. 2008; Janowiak et al. 1998; Janowiak et al. 2010; Roads 2003; Wang et al. 2010a). Reanalysis datasets are produced by a "frozen" model with data assimilation, the process that integrates observations with model simulations, to provide a dynamically consistent analysis for an extended period of time. Unlike the state variables, which are assimilated, precipitation in reanalyses is almost entirely a model product. In some cases, precipitation is assimilated, but weighting of observational information in the analysis procedure is so low that final precipitation products still heavily depend on model physics (Rienecker et al. 2011). So, precipitation in reanalyses can be a metric of model performance in dealing with convective processes, constrained by more realistic weather and climate states than GCMs. The studies for precipitation in reanalyses have also focused on intraseasonal or longer time scales.

To investigate precipitation characteristics as a result of CCEWs and as a source of vertically propagating waves, we extracted the highest available time resolution precipitation products from five reanalyses and the Tropical Rainfall Measuring Mission (TRMM) satellite observations. The spectral analysis for fine time resolution data enables us to access precipitation variability in the context of CCEW activity. By choosing the time frame of 36 days for each spectral analysis set, we can investigate the seasonal evolution of submonthly precipitation variability in different tropical regions.

2. Datasets

We analyzed precipitation data for the period of January 2005 through December 2007 from five reanalyses: ERA-interim (ERA) (Dee et al. 2011), Modern-Era Retrospective Analysis (MERRA) (Rienecker et al. 2011), National Centers for Environmental Prediction (NCEP)-National Center for Atmospheric and Research (NCEP1) (Kalnay et al. 1996), NCEP-Department of Energy (NCEP2) (Kanamitsu et al. 2002), and NCEP-Climate Forecast System Reanalysis (CFSR) (Saha et al. 2010). ERA-interim is the latest reanalysis produced at the European Centre for Medium-Range Weather Forecasts (ECMWF). MERRA is generated by NASA's Goddard Earth Observing System (GEOS) atmospheric model v. 5.2.0 and data assimilation system (DAS). CFSR is the ocean-atmosphere coupled global NCEP reanalysis, an improved version of NCEP1 and NCEP2. The key features and basic information related to precipitation in the reanalyses are listed in Table 1. We used 6-hourly or 3-hourly products, if available, to capture temporal precipitation variability of high-frequency scales.

To compare with the reanalysis results, we used the 3B42 dataset from the Tropical Rainfall Measuring Mission (TRMM) (Huffman et al. 2007). The TRMM 3B42 is a 3-hourly product with the grid resolution of 0.25^ox0.25^o between 50S and 50N. Various satellite measurements were used to generate the precipitation data of 3B42. A combination of the TRMM precipitation radar (PR), the TRMM microwave imager (TMI), and microwave data from other satellites provide precipitation estimates, but there are measurement gaps due to sparse sampling. By using the infrared (IR) channel data from geostationary earth orbit satellites, precipitation estimates were adjusted and covered uniformly in space and time. The final rain products were merged with rain gauge analyses where available.

Although TRMM 3B42 is one of the best high-resolution precipitation datasets, and TRMM monthly precipitation is well validated, we note that it still has uncertainties on subdaily time scales. Using IR brightness temperatures where microwave measurements are unavailable would yield problems with non-convective precipitation. Furthermore, Huffman et al. (2007) described how lack of sensitivity to light precipitation over the ocean in one microwave product has resulted in lower skill in moderate and light rainfall events on subdaily time scales. Nonetheless, their results show TRMM 3-hourly products capture most of the rainfall events observed in a buoy gauge dataset in the western Pacific ITCZ. Histograms of TRMM 3B42 and radar data generally match, and the diurnal cycle of TRMM 3B42 has good agreement with gauge observations with slight phase and amplitude differences.

3. Methodology

We performed a spectral analysis for longitude-time cross sections to identify space-time precipitation variability. This method is especially useful for studying zonally propagating disturbances, giving the spectral dispersion in the wavenumber-frequency space. A power spectrum and variance are proportional to a squared value of precipitation perturbation. Since precipitation is spatially and temporally intermittent, a finer resolution gives higher values of power spectrum and variance. For more reliable quantitative comparisons of variance, we rebinned data in the horizontal to approximately the same resolution of about 1.875^{o}x1.875^{o}. Table 1 shows the available temporal and spatial resolutions of five reanalyses. The spatial rebinning process is not applied to NCEP1, NCEP2, and CFSR, which are already provided at relatively coarse resolution of approximately 1.875^{o}x1.905^{o} in the tropics. We calculate area-weighted average rain rates to rebin the different horizontal resolutions of TRMM, ERA, and MERRA into 1.875^{o}x1.875^{o}. Hourly data from MERRA and CFSR are averaged into the 3-hourly resolution.

Since we are interested in submonthly scale variability and its seasonal changes, the time period of 36 days was chosen for the Fast Fourier Transform (FFT) with 6-day overlap and taper. This time period will resolve westward and eastward IG waves, TD-type waves, MRG waves, most Kelvin waves, and transient parts of the Rossby wave spectrum. The disturbances longer than the monthly scale lie at zero frequency in our wavenumber-frequency spectrum. We define this as the "quasi-stationary" part of the spectrum. Rossby waves have spectral peaks with the periods of 30 days, and the MJO is a 30-90 day intraseasonal oscillation. Thus, the quasi-stationary spectrum is contributed mostly by the MJO and very slowly moving Rossby waves.

Many studies for CCEWs utilize the method of symmetric and anti-symmetric decomposition against the background spectrum to identify wave signals (Hendon and Wheeler 2008; Lin et al. 2006; Wheeler and Kiladis 1999). In these studies, the symmetric component is defined by the average of perturbation variables between the northern and southern hemispheres, and anti-symmetric is half of the difference. Then the symmetric and anti-symmetric spectra are divided by the smoothed background spectrum. Although this method has an advantage in identifying the CCEWs and their phase speeds through the statistically significant dispersion curves in the spectrum, its resultant spectrum only shows relatively significant spectral peaks for meridionally symmetric and anti-symmetric disturbances against the background. On the other hand, the raw spectrum gives absolute variance in Fourier space so that we can compare total precipitation variance as a function of wavenumber and frequency in different datasets. In this paper, we are interested not only in CCEW signals but also in precipitation variability and frequency characteristics. Hence, to evaluate total precipitation variability depending on wavenumber and frequency, we used the raw spectrum without smoothing. To determine whether and how CCEWs are represented in reanalyses, we examine prominent lobes in raw spectra of symmetric and anti-symmetric components.

4. Results

a. Mean precipitation

Fig. 1 shows the spatial distribution of 3-year mean precipitation. All reanalyses have biases in the tropics as pointed out in other studies. ERA and MERRA have almost the same mean value of 0.2 mm/hr, and they share similar characteristics in mean precipitation with consistent positive biases over all tropical regions and over the time series. (See Figs. 1-3.) The mean of NCEP1 is 0.19 mm/hr, which is close to the mean of ERA and MERRA, but it shows a more spatially uniform distribution with less precipitation in the ITCZ compared to other datasets. In contrast, NCEP2 has a significant high bias in the ITCZ. CFSR also has strong precipitation along the ITCZ, but intensified precipitation distributions in the ITCZ are very different between NCEP2 and CFSR. While the positive bias of NCEP2 is significant in the western Pacific, precipitation along the ITCZ in CFSR is exaggerated mainly in the central and eastern Pacific. In Fig. 2, precipitation is averaged over tropical latitudes 15S-15N. Longitude ranges that are mostly land with more than 70% of the total are marked with the black bars in the longitude axis. The dots in the longitude axis represent land-ocean mixed regions, with 30%-70% land. The geographical precipitation patterns of ERA and MERRA look the same except in Africa. ERA and CFSR generate more rainfall than other datasets in Africa, while MERRA shows suppressed rainfall in Africa. Peaks in reanalyses on the west side of America reveal excessive orographic precipitation along the Andes. The time series of zonally averaged precipitation as a function of latitude in Fig. 3 shows the seasonal migration of the ITCZ and the Southern Pacific Convergence Zone (SPCZ). Although there are some biases in mean precipitation (mostly in the ITCZ), all datasets generally agree on the seasonal changes: the ITCZ moves farther to the north at 7N-12N during July-August-September, and strong precipitation in the SPCZ occurs during January-February.

b. Longitude-Time section and PDF

Fig. 4 shows zonal propagation of precipitation at 5N between June-September 2006. Observed TRMM precipitation in Fig. 4a identifies the diurnal cycle and ubiquitous eastward and westward propagating features with different speeds. The large-scale eastward moving envelope is the MJO with the period of 30-90 days. The active phase of the MJO is initiated in the Indian Ocean and progresses through the Maritime Continent and the western Pacific at the speed of 5 m/s. There are also smaller-scale eastward and westward waves within the MJO envelope.

In Fig. 4a, relatively faster eastward moving signals with the phase speed of about 10 m/s are Kelvin waves. Westward signals are composed of TD-type and westward IG waves. Western

African rainfall is dominated by small-scale westward propagating waves, mostly triggered by the diurnal cycle, which are strongly coupled to convection. The diurnal cycle is clearly seen over the land regions.

Figs. 4b-f show the same longitude-time cross sections for reanalyses. Precipitation patterns in ERA, MERRA, and NCEP1 are broadened in space and time. Widespread persistent, weak rainfall is a common problem in climate models. The probability density function (PDF) and the 99th percentile of 3-year precipitation in Fig. 5 shows that intense rainfall events are highly underestimated in ERA, MERRA, and NCEP1. NCEP2, however, has more intense and less persistent precipitation patterns. Westward propagating precipitation features in NCEP2 in Fig. 4e are very strong compared to TRMM, especially in the eastern Pacific. CFSR seems to have the most realistic variability and wave propagation characteristics. The PDF and the 99th percentile of precipitation intensity in CFSR matches the values in TRMM very well in Fig. 5, and the spurious strong westward waves in the Pacific of NCEP2 have become more realistic in CFSR shown in Fig. 4f. We will examine zonal propagation characteristics more closely in the following sections.

c. Spectrum

Fig. 6 illustrates averaged spectra, without filtering or smoothing, between 15S-15N over the time period of 2005-2007. These raw spectra are very “red”, which means spectral density gets higher with lower wavenumber and lower frequency. This “redness” of the spectrum is a universal property of climatic variables. It suggests that the atmospheric processes occur in the broad space and time scales, and that one scale of process is always accompanied by the other scales.

Although the “redness” is an apparent feature of the spectra, we can also identify wave signals in the raw spectra, following preferred lobes in each propagation direction. In Fig. 6, the slopes (frequency/wavenumber) of dotted lines correspond to wave phase speeds, so eastward (westward) propagating disturbances compose the positive (negative) wavenumber spectrum. There is a prominent lobe in the eastward direction with a phase speed of about 14 m/s, which corresponds to the equivalent depth of 20 m, in the TRMM spectrum in Fig. 6a. This is mostly contributed by the Kelvin waves and the eastward IG waves. In the westward direction with negative zonal wavenumbers, the preferred speed depends on the wavenumber and frequency. In the low-frequency range with periods longer than 7 days, the preferred westward phase speed is slowest and corresponds to the equatorial Rossby wave dispersion curve. As the frequency becomes higher, the preferred phase speed increases. At the higher-frequencies with periods shorter than 3 days, the prominent lobe follows along a phase speed of -18 m/s mainly due to westward IG waves. The phase speed of the westward IG wave mode is slightly faster than the value of the eastward IG wave mode. The Doppler shift by the westward zonal wind in the tropical troposphere is considered to be the cause of the directional difference in the preferred phase speeds. The intensified spectrum at the frequency of 1 CPD is due to the diurnal cycle.

Low-frequency large-scale waves including Kelvin, MRG, and Rossby waves can be better illustrated in spectra of the symmetric and anti-symmetric components in Figs. 7 and 8. The symmetric and anti-symmetric spectra of TRMM observations show enhanced power following theoretical dispersion curves of the equatorial shallow water equations with the equivalent depth of 20 m. Kelvin waves are prominent in the symmetric spectrum in Fig. 7a, MRG waves have a signal in the anti-symmetric spectrum in Fig. 8a, and Rossby waves are evident in the both spectra. As Tulich et al. (2011) have shown, observed Rossby waves in the westward spectrum are faster than the theoretical dispersion relation due to background easterlies.

The spectrum of each reanalysis in Figs. 6-9 reveals its own characteristics and drawbacks. As observed in the longitude-time sections in Figs. 4b and 4c, spectra of ERA and MERRA are also similar in Figs. 6b and 6c with weaker spectral densities compared to TRMM (see also frequency characteristics of power spectra in Fig. 9). At lower frequencies shown in Figs. 7b, 7c, 8b, and 8c, preferred phase speeds of Kelvin, MRG, and Rossby waves are the same as TRMM. This suggests that the low-frequency large-scale CCEWs are well represented in ERA and MERRA. However, they are lacking in wave signals at frequencies higher than 1 CPD.

NCEP1 and NCEP2 have spectra only up to 2 CPD due to the limitation of the time resolution. The striking feature of NCEP1 is the very strong diurnal cycle (Figs. 6d, 9d, and 11). Janowiak et al. (1998) reported the overly vigorous diurnal cycle in NCEP1 precipitation by comparing with the Global Precipitation Climatology Project (GPCP), which is a product that combines rain gauge and satellite-derived precipitation. As a complement to this, our spectral analysis has found that the non-migrating diurnal signal near zero wavenumber is especially high, and the migrating diurnal signals are also significant (see Fig. 6d). The diurnal cycle is so strong that it affects the spectral shape making it difficult to see whether any preferred phase speeds exist in NCEP1. The spectral shapes at low frequencies in Figs. 7d and 8d show weak CCEW signals compared to all other datasets. The spectra of NCEP2 in Figs. 6-8e has strong westward signals at all frequencies less than 1 CPD and with a consistent phase speed between -5 m/s and -10 m/s. The different preferred phase speeds in the different wavenumbers and frequencies indicate the properties of dominant wave modes. In the westward direction in NCEP2, it is ambiguous to differentiate the Rossby and IG wave modes since the preferred phase speeds in Figs. 6-8e look the same for these wave modes. Considering the phase speeds of 5-10 m/s in the westward direction, NCEP2 appears to have overly strong TD-type waves, resulting in weak signals on other westward waves. Moreover, MRG waves lack in the anti-symmetric spectrum in Fig. 8e. In the positive wavenumber space in Figs. 6-7e, the Kelvin and eastward IG waves are very weak with slower phase speeds than in TRMM.

The spectra of CFSR in Figs. 6-9f reveals that CFSR has improved skill in producing tropical precipitation in terms of the large-scale waves and diurnal variations. Although CFSR is still lacking in wave signals at frequencies higher than 1CPD, the unrealistic strong westward signal in the low-frequency wave modes seen in NCEP2 has in CFSR become closer to the TRMM spectrum. The weak diurnal peaks in NCEP2 are also enhanced in CFSR to very reasonable values.

More quantitative comparison of diurnal variation is depicted in Fig. 9, which shows the spectrum integrated over all wavenumbers at a given frequency. In ERA and MERRA, the diurnal peaks relative to the background spectra are overestimated compared to TRMM. The extremely exaggerated diurnal signal in NCEP1 is reduced in NCEP2 with the relative peak value less than TRMM. NCEP2 has the weakest relative diurnal peak intensity. The relative diurnal peak intensity in CFSR has a value closest to the TRMM result.

The ratio of the westward to the eastward power spectrum in Fig. 10 shows the frequency dependence of eastward and westward wave activity. Except at periods longer than 25 days affected by the MJO, westward disturbances in TRMM are larger than eastward disturbances. At frequencies lower than 1/3 CPD, all reanalyses overestimate the westward component, suggesting strong low-frequency easterly wave activity in reanalyses. This large ratio is also partly due to the underrepresentation of Kelvin waves in NCEP1, NCEP2, and CFSR as indicated by the symmetric spectra in Fig. 7. Tulich et al. (2012) have concluded that vertical zonal wind shear at low levels, not just the mean flow, is crucial to the direction of convective wave propagation, suggesting the westward bias at lower frequencies in models might be strongly influenced by the unrealistic background shear. At higher frequencies over 0.7 CPD, however, most reanalyses have weaker westward variance, indicating significant model deficiencies in generating high-frequency westward IG waves.

The directional scale-dependent propagation information in precipitation can be gained by integrating spectra within desired spectral bands (Fig. 11). Here, we divided the wavenumber-frequency spectrum into five categories:

- quasi-stationary [eastward and westward with period > 30 days],
- westward_high [westward with frequency > 1/3 CPD (period < 3 days)],
- westward_low [westward with frequency < 1/3 CPD (period > 3 days)],
- eastward_high [eastward with frequency > 1/3 CPD (period < 3 days)], and
- eastward_low [eastward with frequency < 1/3 CPD (period > 3 days)].

The gray color represents the percentage of disturbances with periods longer than the monthly scale. Thus, the MJO and the slowly moving Rossby wave signals with periods longer than 30 days will be in this quasi-stationary category in our study. To the left of the gray color are the westward percentages and to the right are the eastward portions. We distinguished the high frequency from the low frequency with respect to 1/3 CPD (period of 3 days) so that the Kelvin, Rossby, MRG, and TD-type waves are included in the low-frequency category. The contribution of IG waves and the diurnal cycle is included in the high-frequency category. The number in the parenthesis is the percentage of the harmonics of the diurnal cycle, at the frequencies of 1, 2, 3, and 4 CPD, relative to the total variance.

Generally, reanalysis spectra are “redder” than TRMM. This means the spectral densities are more concentrated in the low wavenumbers and low frequencies. The overly red spectra can be interpreted that individual convection events are more persistent in physical space, as discussed in the studies of Ricciardulli and Sardeshmukh (2002) and Tulich et al. (2011) showing higher autocorrelation values from an over-reddened spectrum. In Fig. 11 MERRA has the most persistent tropical precipitation. About 27 % of the total variance in MERRA is contributed by disturbances at scales longer than 30 days, while only 8 % of the variance from TRMM observations is from this quasi-stationary scale. Due to the persistent rainfall in MERRA, the high-frequency variance seems to be sacrificed: total eastward and westward high-frequency variance is only 29 %, which is much lower than the TRMM percentage of 61 %. The choice of the convective parameterization is known to mainly control the mean and variability of precipitation as well as the existence of CCEWs in model simulations. Ruane and Roads (2007) pointed out that the relaxed Arakawa-Schubert scheme tends to have a lack of high-frequency variability in spite of its better performance in interannual variability. Here, we have found the same conclusion for the relaxed Arakawa-Schubert scheme, which has been used in the MERRA GEOS v.5.2.0 assimilation system. ERA shows a better spectral distribution than MERRA, but the low-frequency disturbances are still overestimated. About 30 % of the high-frequency spectrum is contributed by the diurnal cycle in NCEP1. NCEP2 and CFSR have the most reasonable fraction of precipitation variance at the quasi-stationary scale. CFSR’s variance at high frequencies is the most realistic compared to other reanalyses.

d. Regional and Seasonal Variance

Regional distribution of precipitation variance is shown in Fig. 12. The variance is defined by an integral of the inverse FFT of a spectrum. As suggested in the previous sections, variances in ERA, MERRA, and NCEP1 are much smaller than in TRMM. NCEP2 has strong variance along the ITCZ and SPCZ. CFSR has exaggerated variance from the central to eastern Pacific, which is also observed in mean precipitation in Fig. 1f.

The ratio of the high-frequency variance (> 1/3 CPD) to the low-frequency variance (< 1/3 CPD) in Fig. 13 illustrates regional differences in the frequency characteristics. The white color depicts regions where total integrated variance for the high frequency variance is nearly the same as the low frequency variance. A high ratio with red colors in Fig. 13 shows that precipitation in these areas is more influenced by the high-frequency disturbances. In western Africa, TRMM shows up to four times stronger variance in the high-frequency waves than in the low-frequency waves. The convectively coupled IG waves may be the largest contribution of the high-frequency variance. Generally, over land, the impact of high-frequency precipitation variability is most important: the ratio is relatively high over Africa, America and the Maritime Continent (Fig. 13a). Although the ratio along the ITCZ is low compared to the ratio over land, high-frequency variability is still important in the ITCZ areas.

As discussed in the previous section, the high-frequency variability in ERA and MERRA is much weaker than in TRMM. The weakness of these high-frequency variances in ERA and MERRA is a problem over all tropical regions in Fig. 13b and 13c. The lowest value of the mean ratio (See numbers in Fig. 13) in MERRA indicates that MERRA has the most persistent tropical precipitation. The ratios over Africa in all reanalyses, except in CFSR, are significantly lower than the ratio in TRMM. It appears that NCEP1 shows a good regional correlation of the variance ratio with TRMM, but this is because of the strong diurnal cycle in NCEP1 (Fig. 14). In other words, the patterns of the ratios from TRMM and NCEP1 look similar in Fig. 13 for a different reason. Fig. 14 indicates the location of the exaggerated diurnal cycle in each reanalysis. Compared with TRMM, the regional correlation of the diurnal cycle is most reasonable in CFSR, while NCEP2 has weaker variation.

To investigate seasonality of CCEW activity in different wave modes for each tropical region, we divided the tropics into seven regions: Africa, the Indian Ocean, the Maritime Continent, the western Pacific, the eastern Pacific, America, and the Atlantic Ocean. We will mainly discuss seasonal changes in regional precipitation variability from TRMM observations, shown in Fig. 15. Here, we have used the same five categories (quasi-stationary: green, westward_high: dark blue, westward_low: light blue, eastward_high: red, and eastward_low: orange) distinguished by the frequency and the propagation direction as used in Fig. 11.

In TRMM observations, some regions such as Africa, the western and eastern Pacific, and America have obvious seasonal variations. Fig. 15 reveals that westward_high variance is much more significant than variances from other wave modes over all seasons in Africa. Westward_high variance is suppressed during the dry season around December-January-February, and it gets higher for March-April. Then it is suppressed again around June-July. In August westward_high variance shows the most enhanced activity. Since TD-type waves have predominant periods of 3-6 days and IG waves have periods shorter than 3 days, we infer that the strongly enhanced westward_high variance in August corresponds to strong westward IG wave activity influenced by African easterly jet. Tulich et al. (2012) have shown that the composite evolution of TRMM rainfall associated with African mesoscale squall lines is perfectly aligned with filtered anomalies of the westward IG wave band with the phase speed of -18 m/s. His result further supports the idea that African precipitation is greatly affected by westward IG waves.

In TRMM in Fig. 15, America and the Atlantic Ocean have different phases of seasonality from Africa, although some of westward waves in these regions originated in western Africa. It seems that the variance in the Maritime Continent is mainly characterized by the MJO, because the variances of all wave modes generally go with the quasi-stationary variance. It is well known that smaller-scale convective clusters are generated within the active phase of the MJO (Zhang 2005). Thus we expect that strong MJO convective activity results in strong synoptic to mesoscale convective precipitation.

Westward variance dominates the seasonal changes in the western and eastern Pacific Ocean in Fig. 15. The contributions of the eastward and westward disturbances are almost the same during the northern winter, but the westward disturbances of the northern summertime become nearly double the wintertime values. There is a phase difference of precipitation seasonality between the eastern and western Pacific Oceans. The strong westward signal remains until December in the western Pacific Ocean, but it gradually weakens as the season changes in the eastern Pacific Ocean. The dominance of westward_high variance in the Pacific Ocean implies that convection in northern summer is largely influenced by westward IG waves. In contrast to westward variances, eastward variances do not have strong seasonal variations in the Pacific regions like in Africa.

Since westward_high variance dominates the seasonal variation, we further investigate representation of westward_high variability in reanalyses. We find that seasonal enhancement of westward_high variance in different regions in reanalyses generally match the TRMM results. However, in the western Pacific, reanalyses do not reproduce the TRMM annual cycle. It seems that the mechanisms for generation and maintenance of westward_high disturbances in the western Pacific may be different from other regions, and that reanalyses do not represent these. Further studies would be needed.

5. Summary and Conclusions

Using the space-time spectral analysis method, we evaluated submonthly scale variability and CCEW activity of tropical precipitation in five reanalyses. Three-hourly TRMM observations were used as a validation reference to compare reanalysis datasets (3-hourly for ERA, MERRA, and CFSR; 6-hourly for NCEP1 and NCEP2). Besides the common bias among reanalyses, which all show excessive tropical rainfall, the wavenumber-frequency spectrum reveals deficiencies in resolving CCEWs and high-frequency variability. The mean precipitation values and patterns in ERA and MERRA are very similar except in western Africa, and it appears that their regional distributions are close to the distribution in TRMM if the bias is subtracted. The mean of NCEP1 shows weaker rainfall along the ITCZ and more rainfall outside the ITCZ compared to the TRMM patterns. NCEP2 has the largest amount of total precipitation with intense rain along the ITCZ. CFSR produced strong precipitation along the eastern Pacific ITCZ.

The low-frequency CCEWs are relatively well represented in ERA, MERRA, and CFSR, although they have a bias toward the westward direction. The pronounced wave dispersion curves in the spectra of these reanalyses correspond to the TRMM results in the modes of Rossby, MRG, and Kelvin waves. At higher frequencies, however, all the reanalyses have no clear prominent lobes in the spectra, inferring no wave signals. The high-frequency variability in the reanalyses except in CFSR is weaker than in TRMM. Although there is no apparent signal of the convectively coupled IG waves in CFSR, the fraction of high-frequency variance is comparable to TRMM.

CFSR includes many changes since the NCEP2 reanalysis. These include the use of the atmosphere-ocean-land surface-sea ice coupled model with fine horizontal and vertical resolutions, the assimilation of satellite radiances rather than retrievals, and the direct forcing of land hydrology analysis with observed precipitation (Saha et al. 2010). In contrast to CFSR, model-generated precipitation is used for the land forcing in other reanalyses, or pentad precipitation observations are used to nudge soil moisture in NCEP2 (Kanamitsu et al. 2002; Saha et al. 2010). The improvements in precipitation variability in CFSR are likely related to the use of the coupled model with fine resolutions. In addition, improvements of the high-frequency variability and diurnal cycle especially over land suggest that the land surface model changes contribute to the better performance of CFSR. The assimilation of observed precipitation from the daily Climate Prediction Center (CPC) gauge data and pentad CPC merged Analysis of Precipitation (CMAP) datasets seems to have helped the land model performance to become more realistic, and subsequently improved the precipitation product. (Note that the precipitation product in CFSR is still model-derived (Wang et al. 2010b).)

Among five reanalyses, MERRA has the most persistent weak rainfall and very “red” spectrum. Although MERRA’s representation of precipitation climatology has been improved compared to ERA and CFSR (Rienecker et al. 2011), the use of the relaxed Arakawa-Schubert scheme in the GEOS v.5.2.0 model for MERRA seems to result in significant lack of higher-frequency variability. Ruane and Roads (2007) have found that the NCEP seasonal forecast model (SFM) reanalysis, which employs the relaxed Arakawa-Schubert convective parameterization, is also strongly biased toward low-frequency precipitation variability. Indeed, it is a general problem that climate and weather prediction models produce overly persistent light rain, resulting in an over-reddened spectrum (Lin et al. 2006; Ruane and Roads 2007). A more realistic persistence of equatorial precipitation may be achieved by improving subgrid-scale model physics. In nature, convective and mesoscale downdrafts that occur with deep convective updrafts dry the boundary layer and the lower troposphere (Brown and Zhang 1997; Houze and Betts 1981; Lin et al. 2006). In consequence, the development and evolution of subsequent convective events are suppressed. The insufficient representation of this self-suppression mechanism in convective processes is considered one of the primary reasons for the persistent weak tropical rainfall with low variance. Lin et al. (2008) have shown that the use of a stronger convective trigger function also improves tropical precipitation variance. The low criterion for triggering convection entails the initiation of convection easily and generates the drizzling type of precipitation, which in turn contributes to the small variance and over-reddened spectrum.

In addition to the enhancement of the tropical precipitation variance, properly generating spectral peaks associated with CCEWs is also important to simulate the tropical climate. Recent studies have revealed that half of the analyzed GCMs have CCEW signals in the low-frequency spectra but the GCM spectra show faster phase speeds than the observed value (Lin et al. 2006). They concluded that effective static stability is not lowered enough by the diabatic heat released by convection in current GCMs. In ERA, MERRA, and CFSR, the phase speeds of low-frequency waves including Rossby, MRG, and Kelvin waves are very close to the speeds observed in TRMM measurements, but not for the high-frequency waves. It seems that ERA, MERRA, and CFSR can reproduce a realistic signal in low-frequency precipitation with the help of data assimilation of the observed state variables. Although precipitation in reanalyses is a model product, the assimilated control variables such as atmospheric temperature, wind, and humidity constrain the model to generate more realistic precipitation than the GCMs, which entirely depend on the model. At the higher frequencies, precipitation would depend more on the model than on observations due to lack of observations. Hence, the deficiency of high-frequency variability and wave signals in reanalyses may be improved by finer-scale observations and improvements in model physics. To properly resolve CCEWs in models, the rainfall type and its resultant vertical heating profile should be properly represented. Studies have shown that climate models underestimate the stratiform-type "top-heavy heating profile", indicating condensational heating above and evaporative cooling below the melting level (Kiladis et al. 2009; Lin et al. 2004). Misrepresentation of vertical heating profiles would result in inaccurate wave responses, and triggered convection would not be realistic (Ryu et al. 2011).

It is worth of noting that NCEP2 uses a slightly modified version of the simplified Arakawa-Schubert convective parameterization scheme by Pan and Wu (1994) based on Grell (1993) used in NCEP1, but NCEP2 and NCEP1 precipitation differs in many aspects. NCEP2 has enhanced variability and CCEW signals compared to NCEP1, but the phase speeds do not match TRMM presumably due to excessively strong TD-type wave activity in NCEP2. This suggests that the new approach in NCEP2 over NCEP1 is encouraging with respect to resolving equatorial waves and variability, but the model physics still needed to be improved. Unambiguous reasons for the differences in these two reanalyses are not well understood, but it seems that the convective parameterization is not the only important process for correct representation of CCEWs. There have been many attempts to investigate the reasons for lack of CCEWs and precipitation variability in climate models (Frierson et al. 2011; Lin et al. 2008; Lin et al. 2006; Straub et al. 2010; Suzuki et al. 2006). Most studies have concluded that the convective parameterization scheme is the most important factor that determines the existence of CCEW signals in GCMs. Our findings suggest that, along with the convective parameterization scheme, the choice for other model physics such as cloud processes, moist processes in the boundary layer, and the radiation scheme may also play important roles in CCEW activity.

Our understanding and forecasting skill for tropical precipitation processes have been greatly improved due to global observations, advanced models, and growing computer power. This study confirms that the latest reanalyses such as ERA-interim, MERRA, and CFSR have much improved performance in resolving low-frequency CCEWs and precipitation variability over NCEP1 or NCEP2. However, the improved performance in variability are not necessarily accompany with improvements in other skills: CCEW activity and variability are much enhanced in NCEP2 over NCEP1, but the phase speeds are spurious; CFSR shows the best performance in representing diurnal cycle and high-frequency variability, but regional precipitation in the central to eastern Pacific ITCZ is overestimated compared to the western Pacific. Furthermore, the new reanalyses are still very different from observations with respect to variability and CCEW characteristics at high frequencies, meaning deficiencies in short-range forecasts. Since much of tropical precipitation is affected by waves, high-frequency waves should be better represented to produce accurate short-range forecasts. It is hard to determine the relative importance of each factor that interacts with convection in numerical simulations, but we hope that our findings may give useful insights toward understanding the tropical precipitation system and toward improving model physics. Generating realistic precipitation variability especially at high frequencies in global climate models will also indirectly benefit climate prediction by exciting waves that influence feedbacks with the stratosphere.

ACKNOWLEDGEMENTS

We would like to thank George Kiladis for his detailed and helpful comments on the draft. We also thank Julio Bacmeister for his suggestion on the PDF comparison. Comments by two anonymous reviewers greatly helped to improve the manuscript. This work was supported by NASA Ames Research Center contract #NNA10DF70C as part of the Airborne Tropical TRopopause Experiment (ATTREX) under the NASA Science Mission Directorate Earth Venture Program.

REFERENCES

Alexander, M., and J. Holton, 1997: A model study of zonal forcing in the equatorial stratosphere by convectively induced gravity waves. *J. Atmos. Sci.*, **54,** 408-419.

——, 2004: On the spectrum of vertically propagating gravity waves generated by a transient heat source. *Atmos. Chem. Phys.*, **4,** 923-932.

Baldwin, M., and Coauthors, 2001: The quasi-biennial oscillation. *Rev. Geophys.*, **39,** 179-229.

Betts, A., M. Zhao, P. Dirmeyer, and A. Beljaars, 2006: Comparison of ERA40 and NCEP/DOE near-surface data sets with other ISLSCP-II data sets. *J. Geophys. Res.*, **111**, D22S04, doi:10.1029/2006JD007174.

Bosilovich, M., J. Chen, F. Robertson, and R. Adler, 2008: Evaluation of global precipitation in reanalyses. *J. Appl. Meteor. Climatol.*, **47,** 2279-2299.

Brown, R., and C. Zhang, 1997: Variability of midtropospheric moisture and its effect on cloud-top height distribution during TOGA COARE. *J. Atmos. Sci.*, **54,** 2760-2774.

Cho, H., K. Bowman, and G. North, 2004: Equatorial waves including the Madden-Julian oscillation in TRMM rainfall and OLR data. *J. of Climate*, **17,** 4387-4406.

Dee, D., and Coauthors, 2011: The ERA-Interim reanalysis: configuration and performance of the data assimilation system. *Quart. J. Roy. Meteor. Soc.*, **137,** 553-597.

Dickinson, M., and J. Molinari, 2002: Mixed Rossby-gravity waves and western Pacific tropical cyclogenesis. Part I: Synoptic evolution. *J. Atmos. Sci.*, **59,** 2183-2196.

Forster, P., and K. Shine, 2002: Assessing the climate impact of trends in stratospheric water vapor. *Geophys. Res. Lett.*, **29**, 1086, doi:10.1029/2001GL013909.

Frank, W., and P. Roundy, 2006: The role of tropical waves in tropical cyclogenesis. *Mon. Wea. Rev.*, **134,** 2397-2417.

Frierson, D., D. Kim, I. Kang, M. Lee, and J. Lin, 2011: Structure of AGCM-Simulated Convectively Coupled Kelvin Waves and Sensitivity to Convective Parameterization. *J. Atmos. Sci.*, **68,** 26-45.

Hegglin, M., and T. Shepherd, 2009: Large climate-induced changes in ultraviolet index and stratosphere-to-troposphere ozone flux. *Nat. Geosci.*, **2,** 687-691.

Hendon, H., and M. Wheeler, 2008: Some space-time spectral analyses of tropical convection and planetary-scale waves. *J. Atmos. Sci.*, **65,** 2936-2948.

Holton, J., 1972: Waves in equatorial stratosphere generated by tropospheric heat sources. *J. Atmos. Sci.*, **29,** 368-375.

Houze, R., and A. Betts, 1981: Covection in GATE. *Rev. Geophys.*, **19,** 541-576.

Huffman, G., and Coauthors, 2007: The TRMM multisatellite precipitation analysis (TMPA): Quasi-global, multiyear, combined-sensor precipitation estimates at fine scales. *J. Hydrometeor.*, **8,** 38-55.

Janowiak, J., A. Gruber, C. Kondragunta, R. Livezey, and G. Huffman, 1998: A comparison of the NCEP-NCAR reanalysis precipitation and the GPCP rain gauge-satellite combined dataset with observational error considerations. *J. Climate*, **11,** 2960-2979.

Janowiak, J., P. Bauer, W. Wang, P. Arkin, and J. Gottschalck, 2010: An Evaluation of Precipitation Forecasts from Operational Models and Reanalyses Including Precipitation Variations Associated with MJO Activity. *Mon. Wea. Rev.*, **138,** 4542-4560.

Kalnay, E., and Coauthors, 1996: The NCEP/NCAR 40-year reanalysis project. *Bull. Amer. Meteor. Soc.*, **77,** 437-471.

Kanamitsu, M., W. Ebisuzaki, J. Woollen, S. Yang, J. Hnilo, M. Fiorino, and G. Potter, 2002: NCEP-DOE AMIP-II reanalysis (R-2). *Bull. Amer. Meteor. Soc.*, **83,** 1631-1643.

Kawatani, Y., K. Sato, T. Dunkerton, S. Watanabe, S. Miyahara, and M. Takahashi, 2010: The Roles of Equatorial Trapped Waves and Internal Inertia-Gravity Waves in Driving the Quasi-Biennial Oscillation. Part I: Zonal Mean Wave Forcing. *J. Atmos. Sci.*, **67,** 963-980.

Kiladis, G., C. Thorncroft, and N. Hall, 2006: Three-dimensional structure and dynamics of African easterly waves. Part I: Observations. *J. Atmos. Sci.*, **63,** 2212-2230.

Kiladis, G., M. Wheeler, P. Haertel, K. Straub, and P. Roundy, 2009: Convectively coupled equatorial waves. *Rev. Geophys.*, **47**, RG2003, doi:10.1029/2008RG000266.

Lin, J., B. Mapes, M. Zhang, and M. Newman, 2004: Stratiform precipitation, vertical heating profiles, and the Madden-Julian oscillation. *J. Atmos. Sci.*, **61,** 296-309.

Lin, J., M. Lee, D. Kim, I. Kang, and D. Frierson, 2008: The impacts of convective parameterization and moisture triggering on AGCM-simulated convectively coupled equatorial waves. *J. Climate*, **21,** 883-909.

Lin, J. L., and Coauthors, 2006: Tropical intraseasonal variability in 14 IPCC AR4 climate models. Part I: Convective signals. *J. Climate*, **19,** 2665-2690.

Lindzen, R., and J. Holton, 1968: A theory of quasi-biennial oscillation. *J. Atmos. Sci.*, **25,** 1095-1107.

Matsuno, T., 1966: Quasi-Geostrophic Motions in the Equatorial Area. *J. Meteor. Soc. Japan*, **44,** 25-42.

Ricciardulli, L., and P. D. Sardeshmukh, 2002: Local time- and space scales of organized tropical deep convection. *J. Climate*, **15**, 2775-2789

Rienecker, M., and Coauthors, 2011: MERRA: NASA's Modern-Era Retrospective Analysis for Research and Applications. *J. Climate,* **24,** 3624-3648.

Roads, J., 2003: The NCEP-NCAR, NCEP-DOE, and TRMM tropical atmosphere hydrologic cycles. *J. Hydrometeor.*, **4,** 826-840.

Ruane, A., and J. Roads, 2007: 6-hour to 1-year variance of five global precipitation sets. *Earth Interactions*, **11**(11), 1-29.

Ryu, J.-H., M. J. Alexander, and D. A. Ortland, 2011: Equatorial waves in the upper troposphere and lower stratosphere forced by latent heating estimated from TRMM rain rates. *J. Atmos. Sci.*, **68**, 2321-2342.

Saha, S., and Coauthors, 2010: The NCEP climate forecast system reanalysis. *Bull. Amer. Meteor. Soc.*, **91,** 1015-1057.

Solomon, S., K. Rosenlof, R. Portmann, J. Daniel, S. Davis, T. Sanford, and G. Plattner, 2010: Contributions of stratospheric water vapor to decadal changes in the rate of global warming. *Science*, **327,** 1219-1223.

Straub, K., P. Haertel, and G. Kiladis, 2010: An analysis of convectively coupled Kelvin waves in 20 WCRP CMIP3 global coupled climate models. *J. Climate*, **23,** 3031-3056.

Suzuki, T., Y. Takayabu, and S. Emori, 2006: Coupling mechanisms between equatorial waves and cumulus convection in an AGCM. *Dyn. Atmos. Oceans,* **42,** 81-106.

Takayabu, Y. N., and T. Nitta, 1993: 3-5 day-period disturbances coupled with convection over the tropical Pacific Ocean. *J. Meteorol. Soc. Jpn.*, **71,** 221-246.

Tulich, S. N., G. N. Kiladis, and A. Suzuki-Parker, 2011: Convectively coupled Kelvin and easterly waves in a regional climate simulation of the tropics. *Clim. Dyn.,* **36**, 185-203.

Tulich, S. N., and G. N. Kiladis, 2012: Squall lines and convectively coupled gravity waves in the tropics: Why do most cloud systems propagate westward? *J. Atmos. Sci.*, doi:10.1175/JAS-D-11-0297.1, in press.Wallace, J., and V. Kousky, 1968: Observational evidence of Kelvin waves in tropical stratosphere. *J. Atmos. Sci.*, **25,** 900-907.

Wang, J., W. Wang, X Fu, and K.-H. Seo, 2010: Tropical intraseasonal rainfall variability in the CFSR. *Clim. Dyn.,* doi:10.1007/s00382-011-1087-0.

Wang, W., P. Xie, S.-H. Yoo, Y. Xue, A. Kumar, X. Wu, 2010: An assessment of the surface climate in the NCEP climate forecast system reanalysis. *Clim. Dyn.,* doi:10.1007/s00382-010-0935-7

Wheeler, M., and G. Kiladis, 1999: Convectively coupled equatorial waves: Analysis of clouds and temperature in the wavenumber-frequency domain. *J. Atmos. Sci.*, **56,** 374-399.

Yanai, M., and T. Maruyama, 1966: Stratospheric wave disturbances propagating over the equatorial Pacific. *J. Meteorol. Soc. Jpn.*, **44,** 291-294.

Zhang, C., 2005: Madden-Julian oscillation. *Rev. Geophys.*, **43**, RG2003, doi:10.1029/2004RG000158.

TABLES

TABLE 1. Information of five reanalyses analyzed in this study.

	Model Resolution	Available Data Resolution	Model	Convective Parameterization	Reference
ERA (interim)	T255(~79 km), L60	1.5° X 1.5 3-hourly	ECMWF Cy31r2	Tiedtke (1989) and revised by Gregory et al. (2000)	Dee et al. (2011)
MERRA	1/2° X 2/3°, L72	1/2° X 2/3° 1-hourly	Goddard Earth Observing System(GEOS v.5.2.0) atmospheric model and data assimilation system (DAS)	Modified version of the relaxed Arakawa– Schubert convective scheme described by Moorthi and Suarez (1992)	Rienecker et al. (2011)
NCEP1 (NCAR)	T62(~210 km), L28	1.875° X ~1.905° 6-hourly	NCEP Climate Data Assimilation System (CDAS)	Simplified Arakawa-Schubert convective parameterization scheme developed by Pan and Wu (1994) based on Grell (1993)	Kalnay et al. (1996)
NCEP2 (DOE)	T62(~210 km), L28	1.875° X ~1.905° 6-hourly	NCEP Climate Data Assimilation System (CDAS)	Minor tuning of the same convective parameterization as in NCEP1	Kanamitsu et al. (2002)
CFSR	T382(~38 km), L64	0.313° X ~0.312° 1.875° X ~1.905° 1-hourly 6-hourly	Atmosphere (GFS) – ocean (MOM4, Noah) coupled model [GSI (atmosphere), GODAS with MOM4 (ocean and sea ice), and GLDAS and Noah model (land) were used for analyses.]	Simplified Arakawa-Schubert convection with momentum mixing	Saha et al. (2010)

FIGURE CAPTIONS

FIG. 1. Tropical mean precipitation (mm/hr) in 2005-2007 for (a) TRMM, (b) ERA, (c) MERRA, (d) NCEP1, (e) NCEP2, and (f) CFSR.

FIG. 2. Averaged precipitation over the latitude of 15S-15N. Longitude ranges that are mostly land with more than 70% of the total are marked with the black bars in the longitude axis. The dots in the longitude axis represent land-ocean mixed regions, with 30%-70% land.

FIG. 3. Time series of monthly zonal mean precipitation (mm/hr).

FIG. 4. Longitude-time section of precipitation (mm/hr) at the latitude of 5N between June-September 2006. Land regions are denoted by black bars in the longitude axis.

FIG. 5. The probability density function (PDF) of precipitation between 15S-15N over 2005-2007.

FIG. 6. Averaged wavenumber-frequency power spectrum of precipitation between 15S-15N over 2005-2007. Phase speed lines of -5, -10, -18, and 14 m/s are plotted with dotted lines.

FIG. 7. Averaged symmetric wavenumber-frequency power spectrum of precipitation between 15S-15N over 2005-2007. The curves correspond to theoretical dispersion relations of equatorial shallow water equations with the equivalent depth of 20 m. Note that the ranges of wavenumber and frequency are different from Fig. 6.

FIG. 8. Similar to Fig. 7, except for the anti-symmetric spectrum

FIG. 9. Integrated power spectrum of precipitation over wavenumbers.

FIG. 10. The ratio of the westward to the eastward power spectrum.

FIG. 11. Percentage of the power spectrum categorized into five groups: quasi-stationary [eastward and westward with period > 30 days], westward_high [westward with frequency > 1/3 CPD (period < 3 days)], westward_low [westward with frequency < 1/3 CPD (period > 3 days)], eastward_high [eastward with frequency > 1/3 CPD (period < 3 days)], and eastward_low [eastward with frequency < 1/3 CPD (period > 3 days)]. The contribution of the diurnal cycle is included in the high-frequency category. The number in the parenthesis is the percentage of the harmonics of the diurnal cycle, at the frequencies of 1, 2, 3, and 4 CPD, relative to the total variance.

FIG. 12. Precipitation variance (mm^2/hr^2) calculated from an integral of the inverse FFT of a spectrum.

FIG. 13. Ratio of the high-frequency (periods < 3 days) variance to the low-frequency (periods > 3 days) variance.

FIG. 14. Normalized variance of the diurnal cycle and harmonics.

FIG. 15. Time series of TRMM regional precipitation variance (mm^2/hr^2) categorized according to propagation directions and frequency (westward_high: dark blue, westward_low: light blue, quasi-stationary: green, eastward_low: orange, and eastward_high: red).

FIGURES

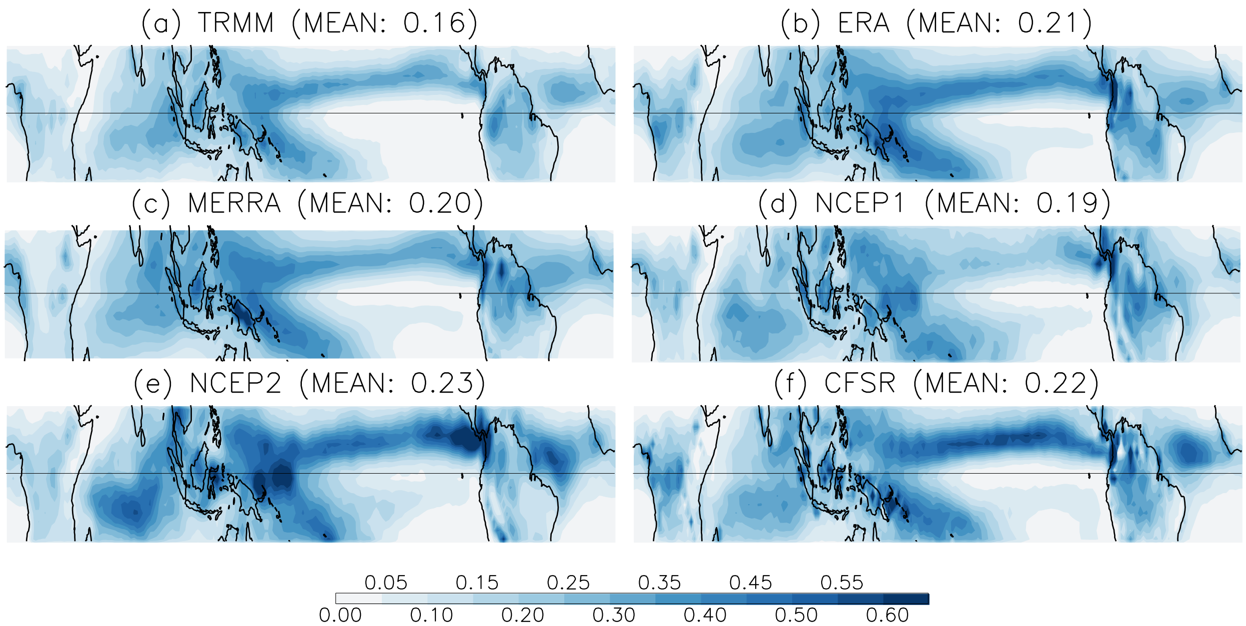

FIG. 1. Tropical mean precipitation (mm/hr) in 2005-2007 for (a) TRMM, (b) ERA, (c) MERRA, (d) NCEP1, (e) NCEP2, and (f) CFSR.

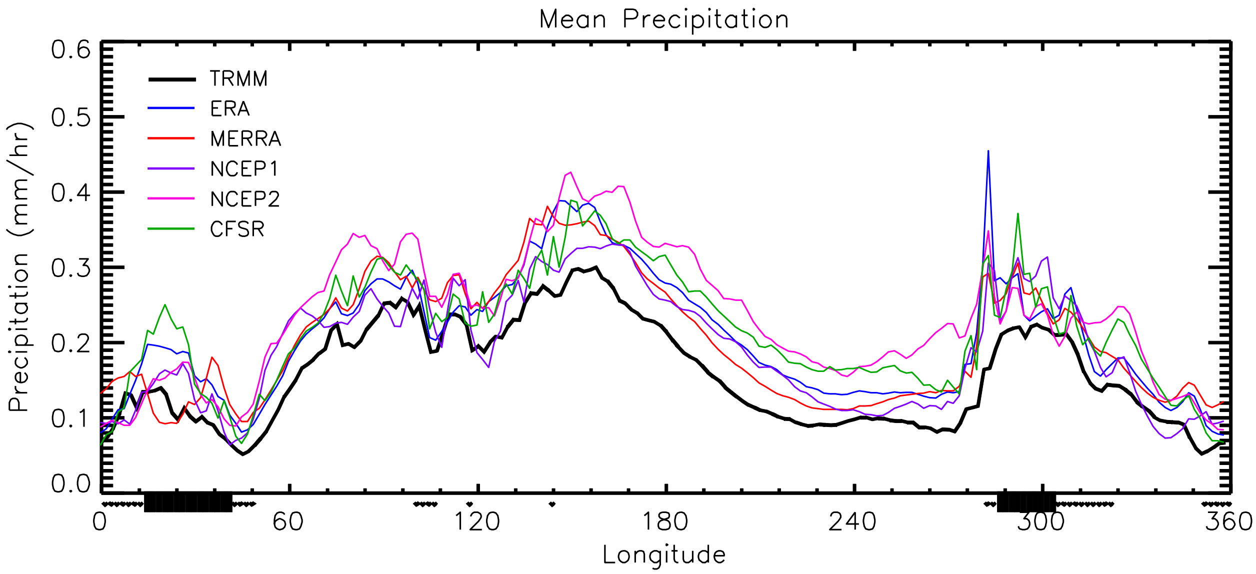

FIG. 2. Averaged precipitation over the latitude of 15S-15N. Longitude ranges that are mostly land with more than 70% of the total are marked with the black bars in the longitude axis. The dots in the longitude axis represent land-ocean mixed regions, with 30%-70% land.

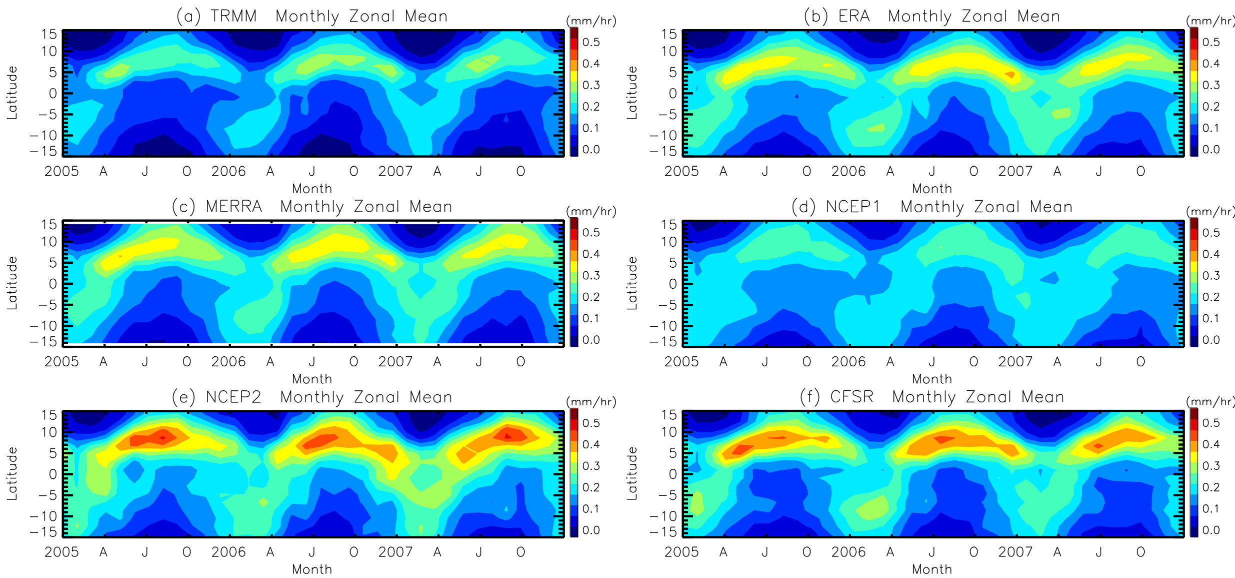

FIG. 3. Time series of monthly zonal mean precipitation (mm/hr).

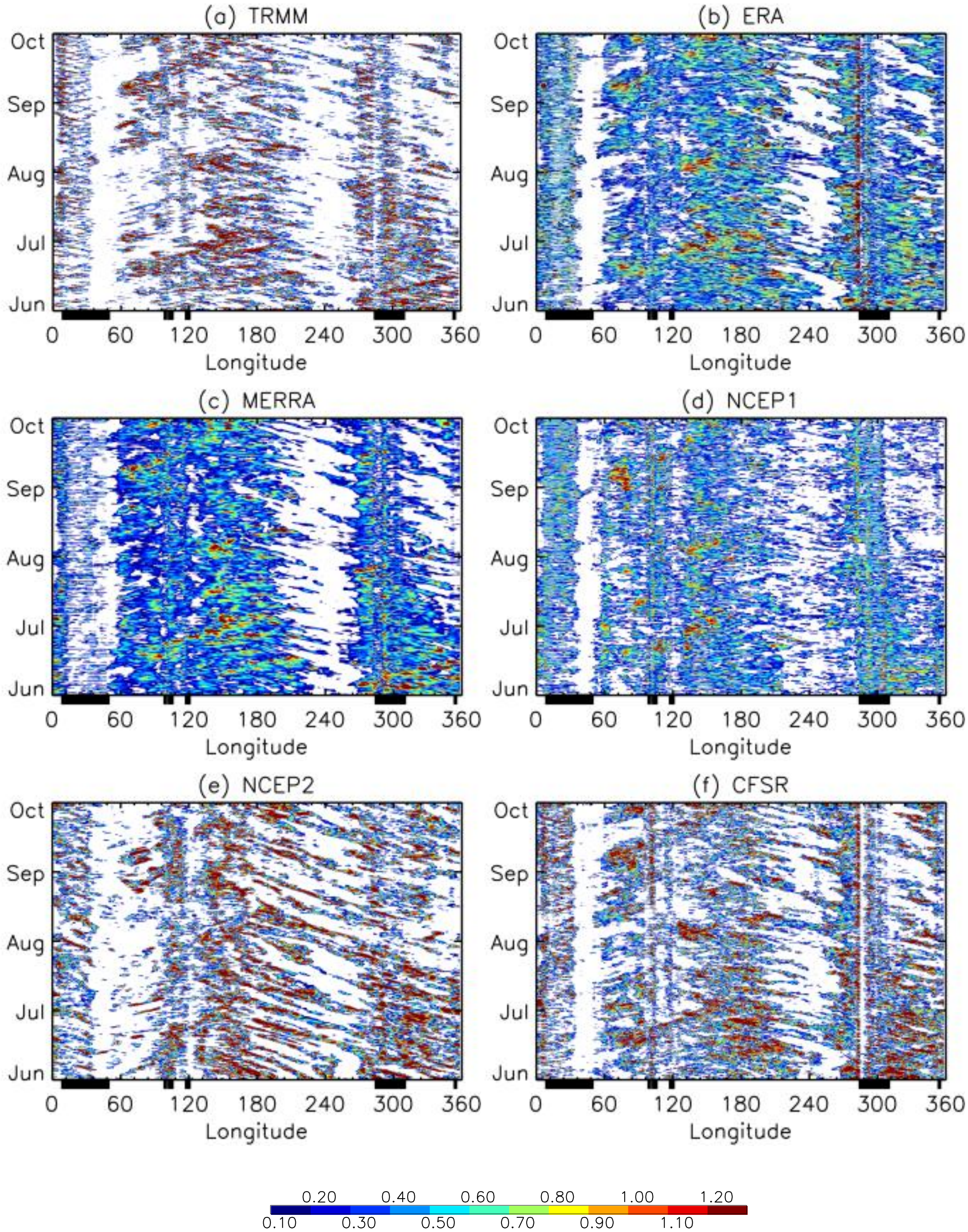

FIG. 4. Longitude-time section of precipitation (mm/hr) at the latitude of 5N between June-September 2006. Land regions are denoted by black bars in the longitude axis.

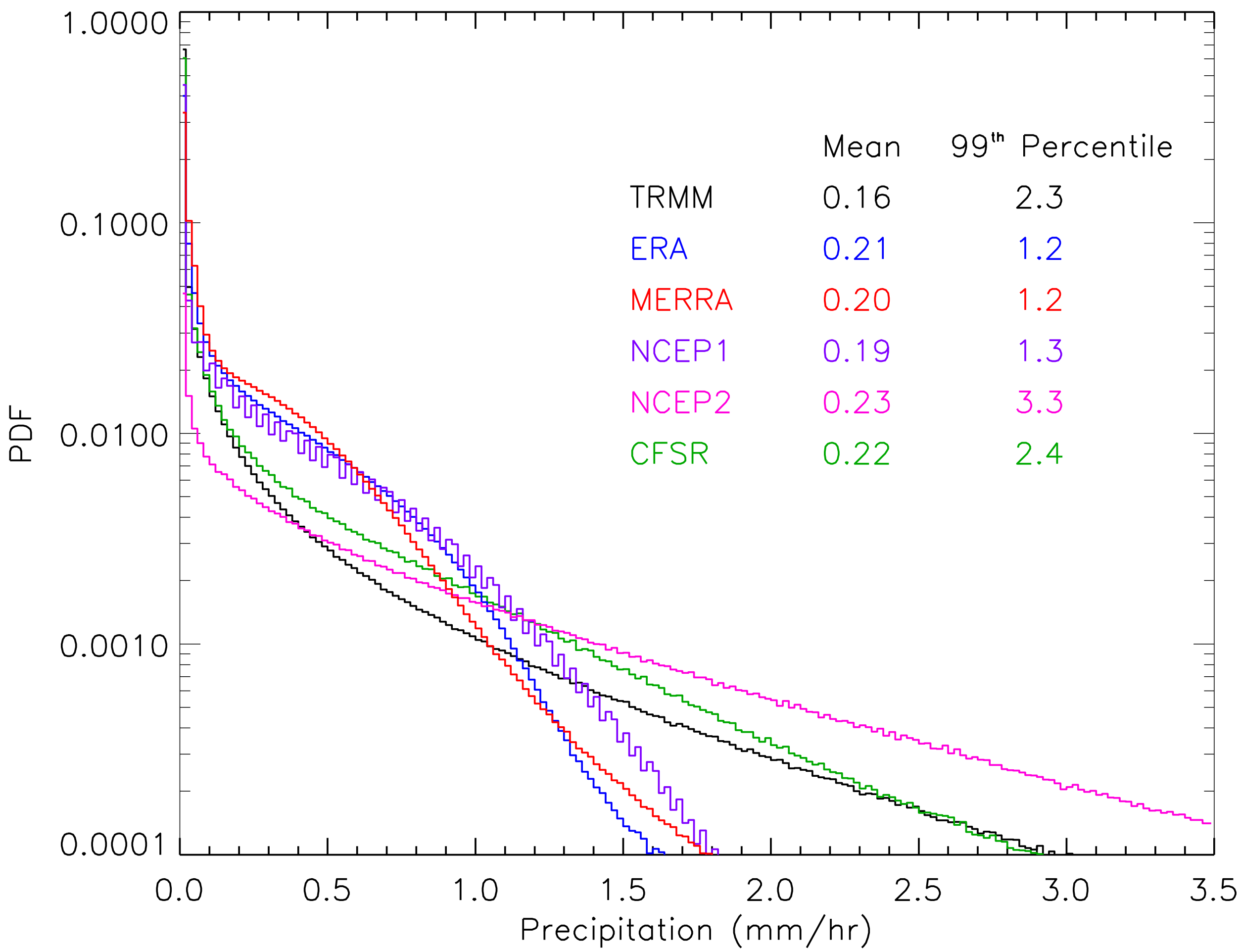

FIG. 5. The probability density function (PDF) of precipitation between 15S-15N over 2005-2007.

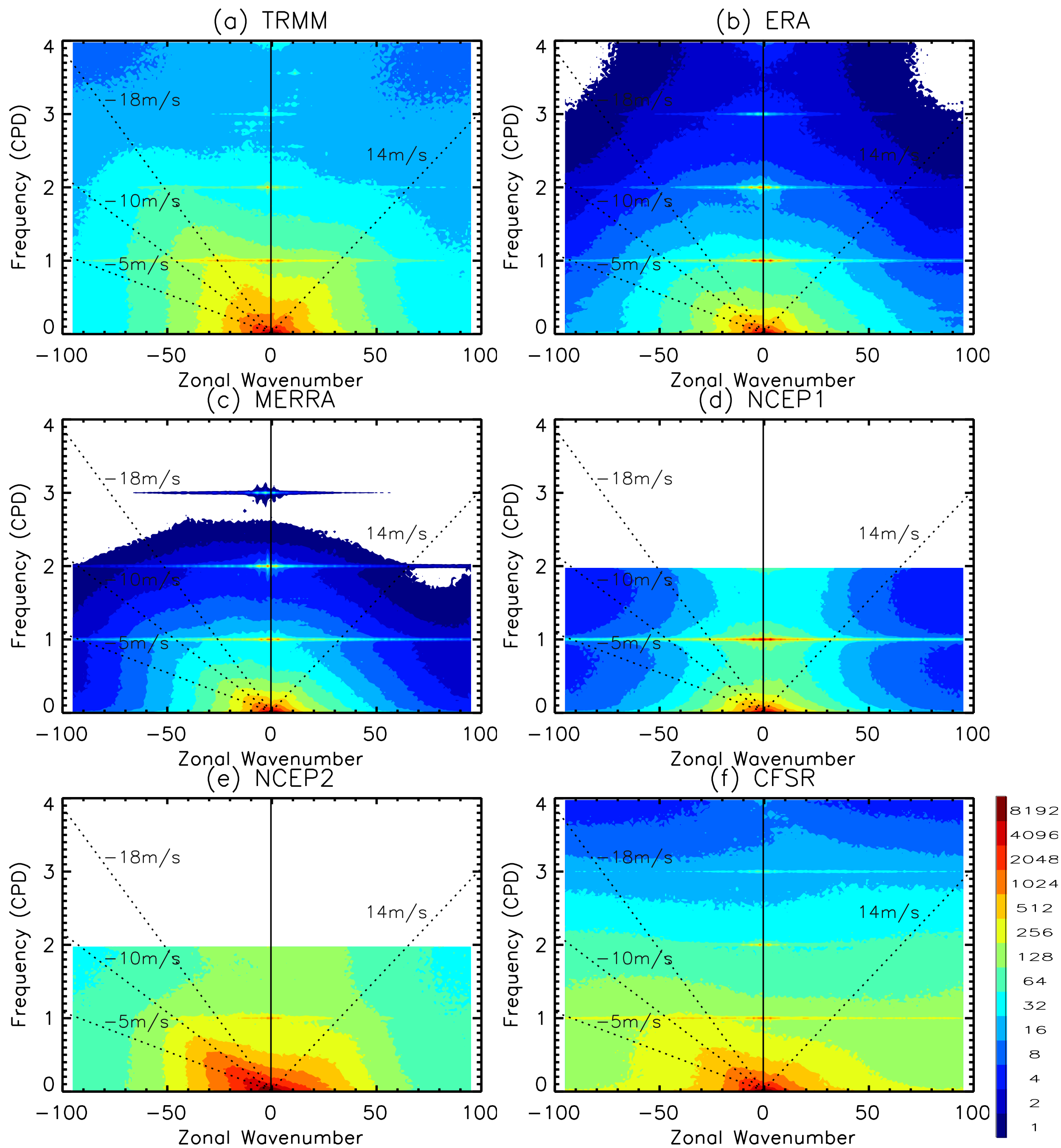

FIG. 6. Averaged wavenumber-frequency power spectrum of precipitation between 15S-15N over 2005-2007. Phase speed lines of -5, -10, -18, and 14 m/s are plotted with dotted lines.

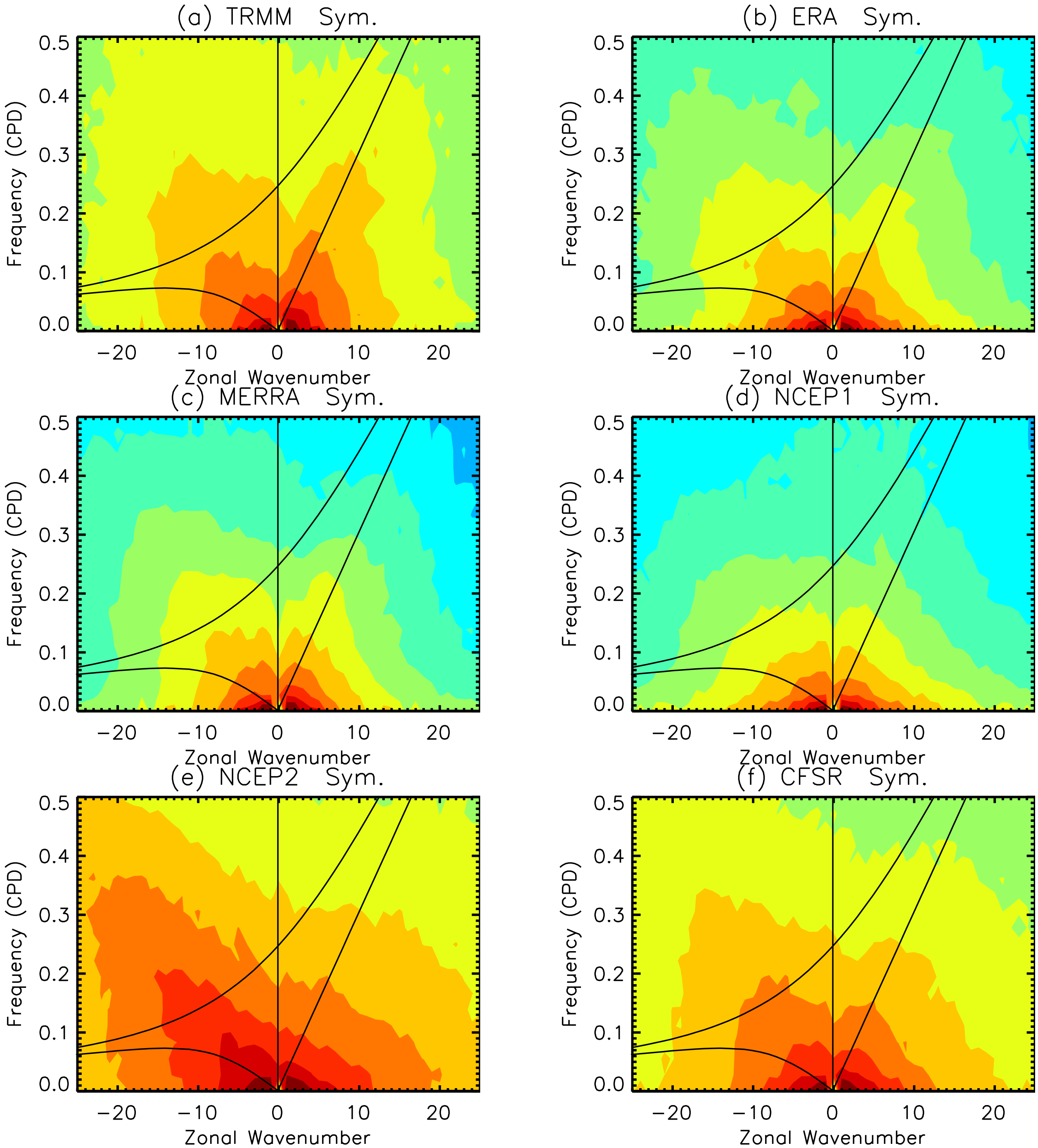

FIG. 7. Averaged symmetric wavenumber-frequency power spectrum of precipitation between 15S-15N over 2005-2007. The curves correspond to theoretical dispersion relations of equatorial shallow water equations with the equivalent depth of 20 m. Note that the ranges of wavenumber and frequency are different from Fig. 6.

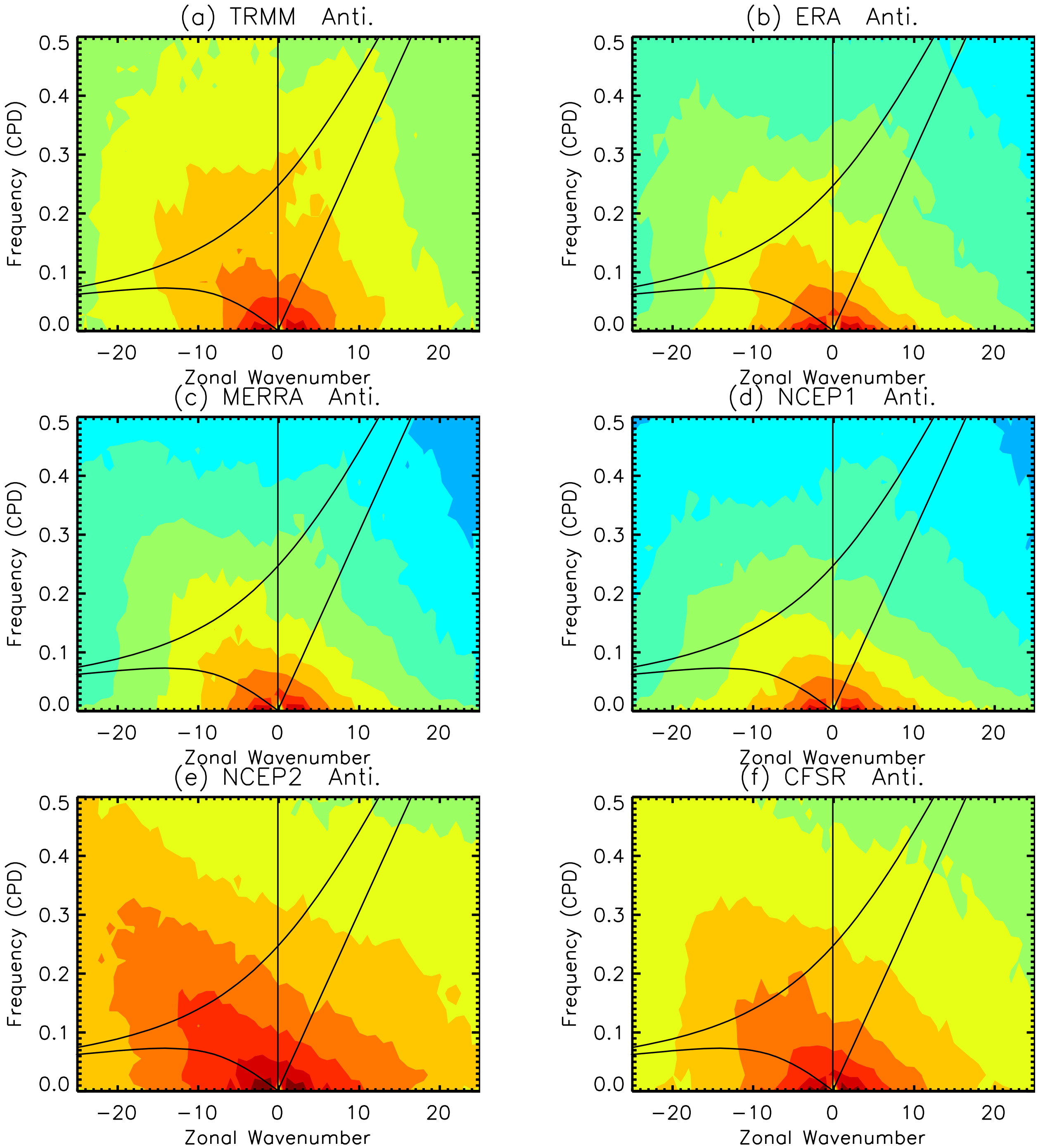

FIG. 8. Similar to Fig. 7, except for the anti-symmetric spectrum

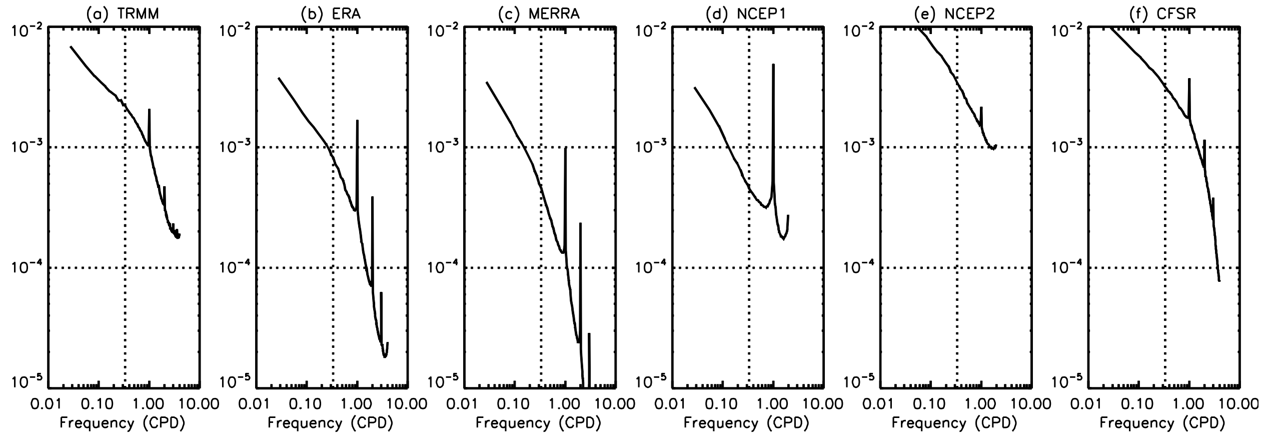

FIG. 9. Integrated power spectrum of precipitation over wavenumbers.

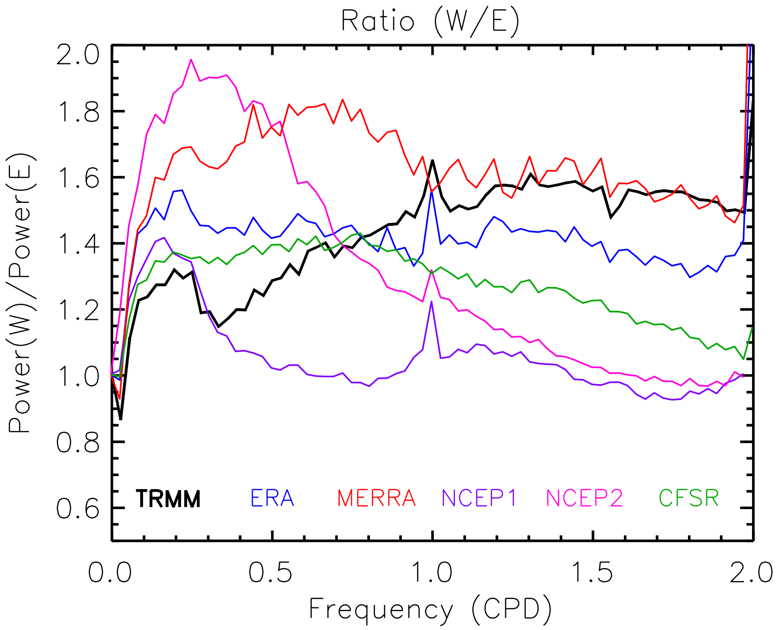

FIG. 10. The ratio of the westward to the eastward power spectrum.

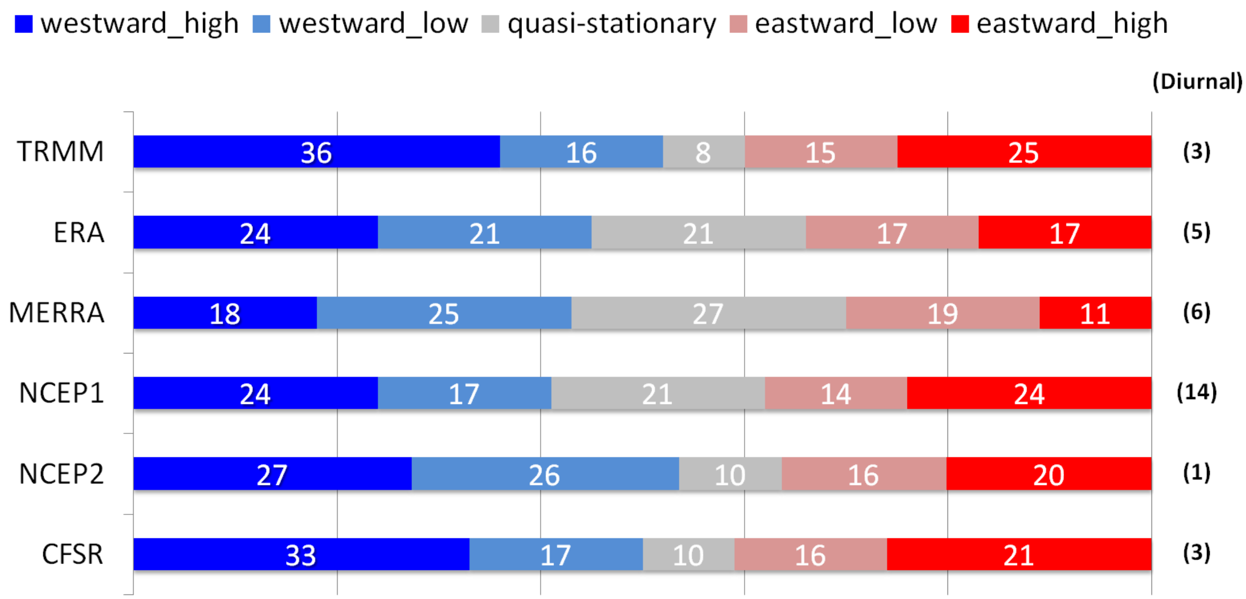

FIG. 11. Percentage of the power spectrum categorized into five groups: quasi-stationary [eastward and westward with period > 30 days], westward_high [westward with frequency > 1/3 CPD (period < 3 days)], westward_low [westward with frequency < 1/3 CPD (period > 3 days)], eastward_high [eastward with frequency > 1/3 CPD (period < 3 days)], and eastward_low [eastward with frequency < 1/3 CPD (period > 3 days)]. The contribution of the diurnal cycle is included in the high-frequency category. The number in the parenthesis is the percentage of the harmonics of the diurnal cycle, at the frequencies of 1, 2, 3, and 4 CPD, relative to the total variance.

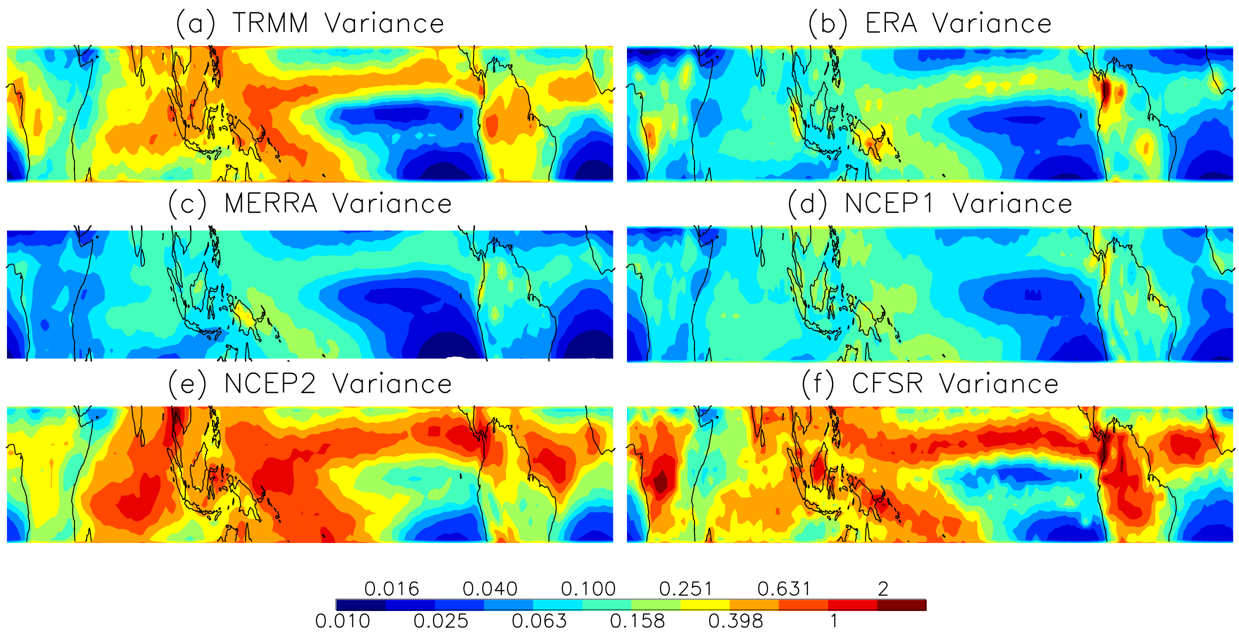

FIG. 12. Precipitation variance (mm^2/hr^2) calculated from an integral of the inverse FFT of a spectrum.

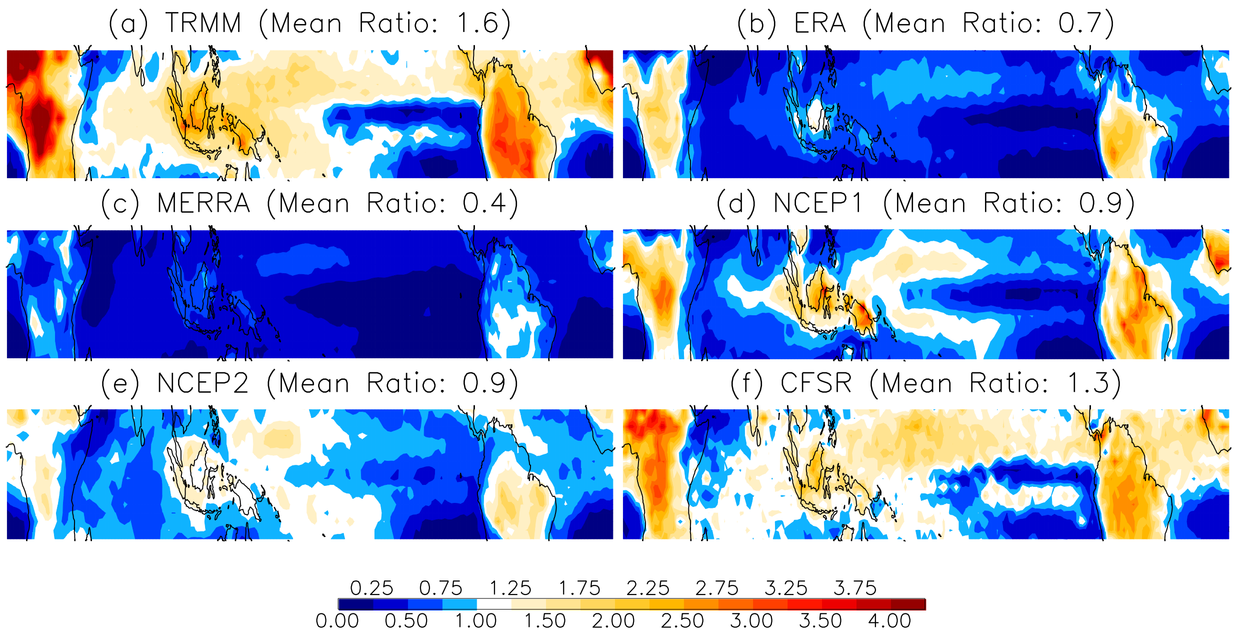

FIG. 13. Ratio of the high-frequency (periods < 3 days) variance to the low-frequency (periods > 3 days) variance.

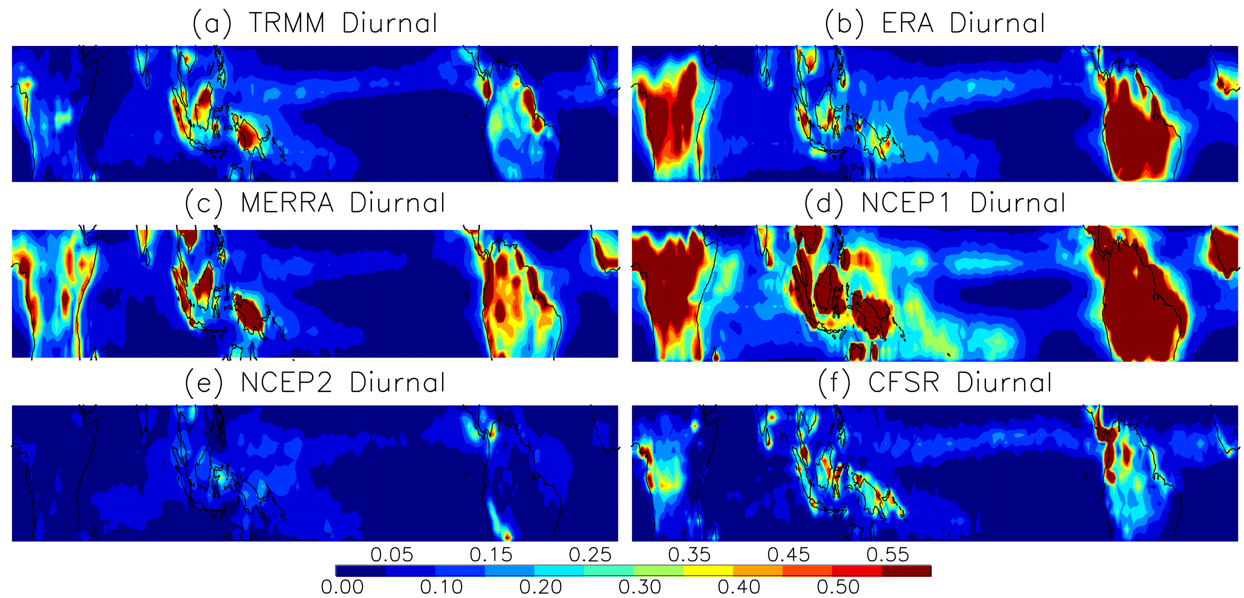

FIG. 14. Normalized variance of the diurnal cycle and harmonics.

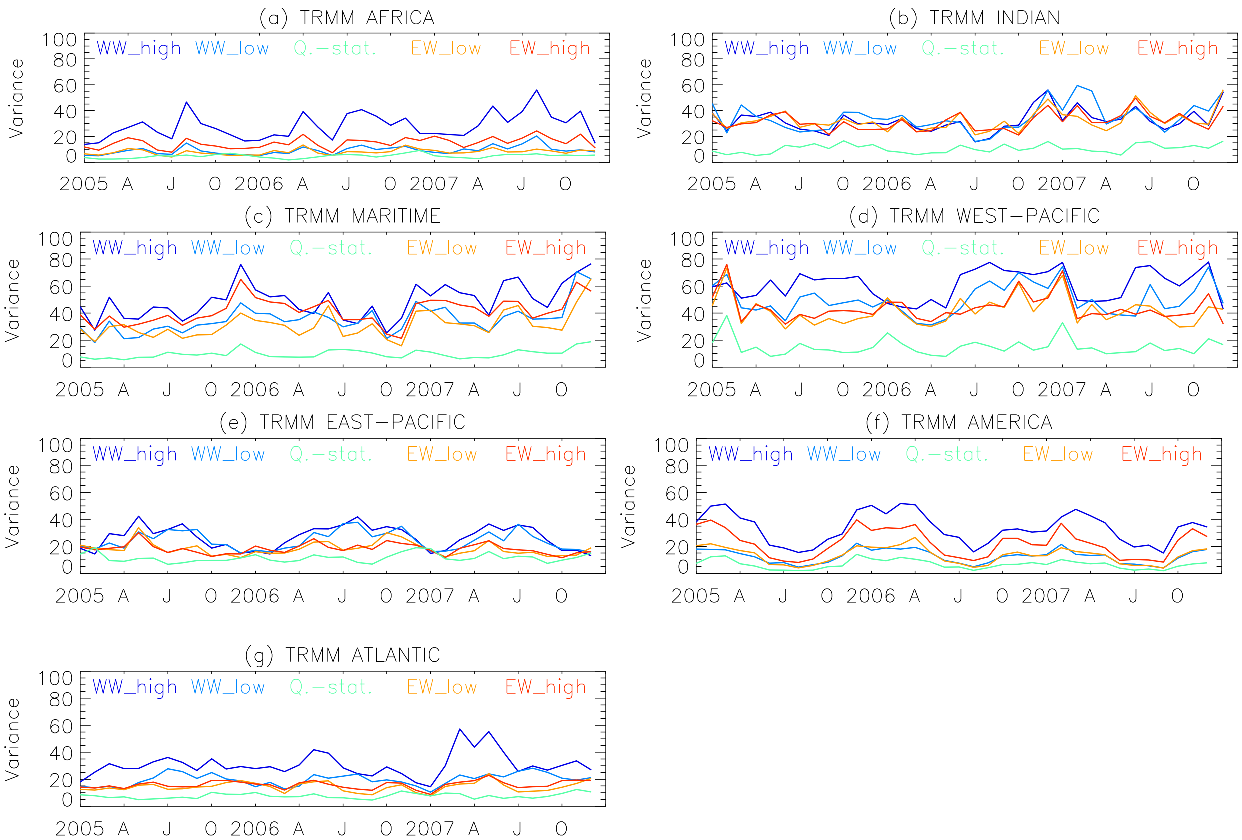

FIG. 15. Time series of TRMM regional precipitation variance (mm^2/hr^2) categorized according to propagation directions and frequency (westward_high: dark blue, westward_low: light blue, quasi-stationary: green, eastward_low: orange, and eastward_high: red).